INTERNATIONAL JOURNAL FOR NUMERICAL METHODS IN FLUIDS, VOL. 16, 259–285 (1993)

ANALYSIS OF EROSION BEHAVIOUR IN A TURBOCHARGER RADIAL TURBINE

A. C. BENIM AND H. G. NEUHOFF

R&D Thermal Machinery Dept., ABB Turbo Systems Ltd., CH-5401 Baden, Switzerland

SUMMARY

An analysis of the erosion behaviour of a turbocharger radial turbine is presented. The solution domain includes both sides of the radial turbine scroll with double intake and the rotor channel. In the analysis a dilute gas–particle flow assumption is employed. The gas turbulence is defined by the k–ε model. In solving the gas phase equations, the computer code Harwell-FLOW3D is employed, which is based on a finite volume formulation using non-orthogonal body-fitted structured gridding and a pressure correction method. The particle phase is described by a Lagrangian approach, while particle paths are computed deterministically, neglecting the turbulent dispersion. For the computation of particle trajectories the code PTRACK is employed, which has been developed at ABB. Computations are carried out for several particle size classes. The results show that particles are thrown back into the scroll by the rotor at high rates. This seems to be the main source of erosion effects in the scroll. It has been observed that particles are unequally distributed between the scroll sides on their re-entry, resulting in greater erosion on one of the scroll sides. The maximum erosion along the scroll is found to be likely to occur near the scroll end.

KEY WORDS Turbocharger radial turbine Gas–particle flow Erosion

INTRODUCTION

The concept of turbocharging is being extensively employed in reciprocating combustion engines. Combustion gases led into the turbocharger contain solid particles (soot, fly ash) which may cause erosion damage in various component parts. The prevention of erosion damage requires a detailed understanding of the fluid dynamics in the turbocharger. This is certainly not a straightforward issue, since the flow situation is quite complex owing to the two-phase flow, turbulence, compressibility and three-dimensional complicated geometry. Recent developments in CFD procedures are, however, encouraging, since they allow prediction of complex flow situations with increasing realism. Hence the purpose of the present study is to investigate the fluid dynamics and erosion behaviour in turbochargers by means of state-of-the-art CFD procedures.

The problem of erosion is common to many applications of turbomachinery and other multiphase flow industrial devices and has attracted the continuous attention of researchers for several decades.[1]

A numerical investigation of the particle dynamics in the turbine environment was presented by Hussain and Tabakoff.[2,3] In this model an inviscid flow was assumed. Furthermore, the flow field was represented by a two-dimensional blade-to-blade solution at the mean radius, making the procedure unsuitable for significant hub and tip contouring and large radial variations.[1–4]

0271 2091/93/040259–27$18.50

Received January 1992
Revised September 1992

Hamed[4] extended this procedure for substantial variations in hub and tip contours in the axial direction, computing the flow field at the two-dimensional curved hub-to-tip stream surface at mid-channel.

Predictions of particle tracking and erosion based on two- and three-dimensional computations of the flow field in turbomachinery components were presented by Mengütürk and Sverdrup[5] and Günes and Mengütürk.[6] In these studies an inviscid flow assumption was again made.

In previous work on the prediction of erosion damage in turbines and compressors, axial flow machines have mostly been considered. Radial flow machines have received relatively little attention. In a recent study by Tabakoff and Hamed[7] a radial compressor was investigated. The situation in the radial turbine is quite different from that in the compressor. In the radial turbine the centrifugal force due to rotation acts against the flow direction, causing some particles to turn back into the scroll, necessitating an integrated treatment of the scroll and the rotor. An investigation of a radial turbine was also presented by Tabakoff and Hamed[8] assuming an inviscid flow field and using the quasi-three-dimensional procedures mentioned above.[2-4]

Particle trajectory calculations considering a fully three-dimensional, viscous, turbulent flow are already known.[9-11] However, these applications are found in the related fields of process engineering rather than in turbomachinery. In such applications, trajectories of particles within the fluid are of most importance, whereas impacts with component parts and erosion damage are not investigated, being less important or irrelevant.

The present study demonstrates a completely three-dimensional investigation of the gas–particle flow and erosion damage in a turbocharger radial turbine, wherein the modelling of gas and particle flows is equally emphasized, obtaining the flow field by solving the three-dimensional Navier–Stokes equations for turbulent flow. Furthermore, we believe that we are also presenting a more detailed analysis of the particle motion in the scroll–rotor system compared with previous work of other authors[8] predicting similar phenomena.

MODELLING THE TWO-PHASE FLOW

In the analysis it is assumed that the gas flow remains unaltered by the particle motion. This enables the gas flow to be computed once and for all, without considering any interaction with the particle phase, and particle trajectories can subsequently be computed on the basis of the gas velocity field obtained by the first step. This assumption is valid for low particle loads ($< 10\%$).[12]

Modelling the fluid flow

For the fluid flow computations the code Harwell-FLOW3D[13] is employed, which is a general-purpose CFD code based on a finite volume formulation using non-orthogonal body-fitted structured grids and a pressure correction method.

In modelling the gas phase, the k–ε model is employed as the turbulence model. Convective terms are discretized using the HYBRID scheme. The Navier–Stokes equations are solved by a pressure correction method. In the present method the SIMPLEC algorithm has been used.

For wall boundaries, no-slip conditions hold, while the momentum exchange with the wall is modelled by a wall function approach. For the energy equation, adiabatic wall boundary conditions are applied. At outlet boundaries, normal gradients of all convective–diffusively transported variables are prescribed as zero. In computing the flow in the rotor channel, periodic boundaries also appear. Conditions along these boundaries are prescribed to be identical between each pair.

Modelling the particle motion and erosion damage

Particle motion is computed by the code PTRACK developed at ABB[14,15] in a manner compatible with FLOW3D. It employs a Lagrangian description of the particle phase, which provides a more straightforward means of modelling impact mechanisms and erosion damage than the Eulerian approach.

In the particle equations of motion, only the fluid drag is considered. A spherical particle form is assumed. Furthermore, the fluid drag is computed using the mean fluid velocity field, neglecting the turbulent fluctuations. Forces due to interaction of particles (particle–particle collisions) are also not modelled, making the procedure applicable to dilute gas–particle flows.

Under the above-mentioned assumptions the equations of particle motion can be expressed in general form as

$$\frac{du_P}{dt}=\frac{1}{T_{PR}}(u_G-u_P), \tag{1}$$

$$\frac{dv_P}{dt}=\frac{1}{T_{PR}}(v_G-v_P)+\gamma\frac{w_P^2}{r_P}+\lambda(2w_P\Omega+\Omega^2 r_P), \tag{2}$$

$$\frac{dw_P}{dt}=\frac{1}{T_{PR}}(w_G-w_P)-\gamma\frac{v_P w_P}{r_P}-\lambda 2\Omega v_P, \tag{3}$$

$$\frac{dx_{1,P}}{dt}=u_P, \qquad \frac{dx_{2,P}}{dt}=v_P, \qquad \frac{dx_{3,P}}{dt}=(1-\gamma)w_P+\gamma\frac{w_P}{r_P}. \tag{4}$$

Recall that in equations (1)–(3) the gas velocity components represent only the local time-mean values, neglecting the effect of turbulent fluctuations.[1,10] The particle relaxation time (equations (1)–(3)) is given by

$$T_{PR}=\frac{\rho_P d_P^2}{0{\cdot}75\,\mu C_D Re_P}, \tag{5}$$

with the particle Reynolds number computed from

$$Re_P=\frac{\rho_G d_P C_{REL}}{\mu}, \tag{6}$$

where

$$C_{REL}=\sqrt{[(u_G-u_P)^2+(v_G-v_P)^2+(w_G-w_P)^2]}. \tag{7}$$

For the drag coefficient in (5), various expressions exist in the literature. In the present study the following relations taken from Reference 16 are employed:

$$C_D=\begin{cases}0{\cdot}44 & \text{for } Re_P\geqslant 1000,\\ (24/Re_P)\ (1+0{\cdot}15\,Re_P^{0{\cdot}687}) & \text{for } Re_P<1000.\end{cases} \tag{8}$$

The particle equations of motion are integrated using Gear's method.[11,14,15] Further details about the modelling of particle motion with PTRACK are given in References 14 and 15.

The modelling of the impact mechanism is of ultimate importance for the prediction of erosion. In the present analysis a model proposed by Tabakoff and Hamed[7] is implemented. In this method the rebound characteristics are calculated using experimentally determined restitution

ratios for normal and tangential components of the velocity. These relations can be expressed as

$$U'_{\mathrm{N}} = -\alpha_{\mathrm{N}} U_{\mathrm{N}}, \tag{9}$$

$$U'_{\mathrm{T}} = \alpha_{\mathrm{T}} U_{\mathrm{T}}, \tag{10}$$

where

$$\alpha_{\mathrm{N/T}} = \sum_{M=1}^{4} (a_{\mathrm{N/T}})_M \, \beta^{(M-1)}. \tag{11}$$

According to equations (9) and (10), not only the normal component but also the tangential component of the particle velocity is altered by an impact. The restitution ratios, which take different values for the normal and tangential components, are expressed by equation (11). From equation (11) one can see that the restitution ratios are modelled assuming a third-order polynomial dependence on the particle approach angle β. The coefficients $a_{\mathrm{N/T}}$ of the polynomials are empirically determined values which depend on material properties.

In formulating the erosion damage, the model of Tabakoff and Hamed[7] has again been used. According to this model, the erosion parameter giving the mass of the eroded target material per mass of impinging particles can be expressed as

$$\varepsilon = A_1[1 + A_2 \sin(A_3\beta)]^2 \, U^2 \cos^2\beta \, [1 - (1 - A_4 U \sin\beta)^2] + A_5 \, (U \sin\beta)^4, \tag{12}$$

where U is the particle speed before impact and the coefficients A_i are empirically determined constants depending on material properties.

THE SOLUTION DOMAIN AND ITS PARTITIONING

The geometry of the related component parts of the investigated turbocharger is illustrated in Figure 1. This drawing is neither true to scale nor does it include the details of the real construction. It serves merely to give a qualitative image of the three-dimensional arrangement. As can be seen from Figure 1, the whole domain of interest consists of the two sides of the double-sided radial turbine scroll and the rotor channel. All component parts show strongly three-dimensional shapes (Figure 1).

The most straightforward way of treating the problem is to partition the whole domain into three subdomains (Figure 1), namely the two sides of the scroll and the rotor channel. Computations are carried out for both scroll sides separately, specifying standard boundary conditions at their outlets. The rotor channel is subsequently computed, prescribing the computed outlet values of the scroll sides from the previous step as inlet boundary conditions. The disadvantage of such a treatment is the neglect of the interaction between subdomains. This problem could be circumvented by employing more sophisticated techniques. However, the present approach is adapted here as a first approximation.

In modelling the flow in the rotor channel, only one circumferential sector between two blades is considered. At the boundaries of this sector in the circumferential direction, periodic conditions are applied. In deriving the inlet boundary conditions for this channel sector, the circumferentially averaged values from the scroll solution are used. In doing so, the eventual unsteadiness of the flow relative to the rotor due to the non-uniform inflow conditions along the circumferential direction is ignored.

COMPUTATIONAL GRIDS

For each scroll side a $59 \times 20 \times 20$ grid is employed, the figure 59 indicating the number of divisions along the scroll length. Figure 2 shows several sections of the 3D grid for the turbine side

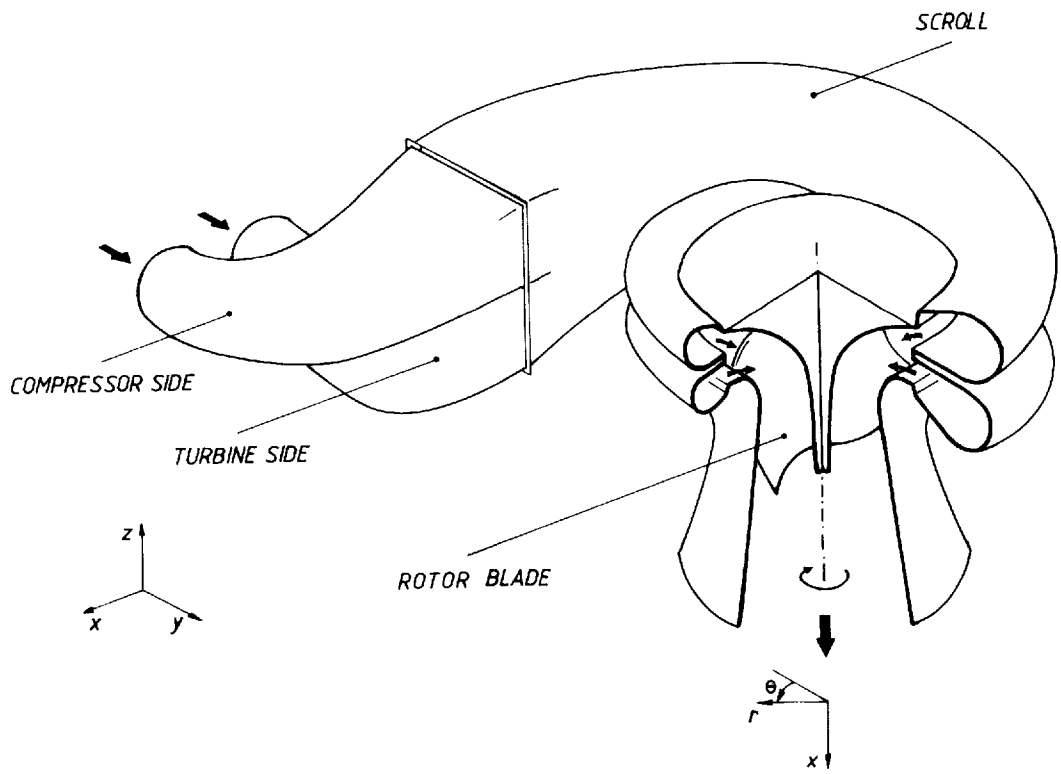

Figure 1. Geometry

(TS) of the scroll. One can see (section C–C) that the scroll outlet has been modified by adding a channel-like outlet section. This has been done for computational convenience in order to be able to apply the standard outlet boundary conditions. Obviously, the zero-gradient conditions are not very adequate in this radial inflow situation. However, in order to reduce the effect of improper outlet conditions, the inlet values for the rotor channel are evaluated at the original scroll outlet, ignoring the modified extension.

The grid for the rotor channel (RC) has 54 cells in the axial, 23 in the radial and 19 in the circumferential direction. Figure 3 shows a meridional and two blade-to-blade sections of the generated 3D grid. These drawings represent orthogonal projections of the curved grid surfaces. In the circumferential direction the boundaries do not extend up to the next blade but are placed at mid-channel positions between adjacent blades.

FLOW COMPUTATION

Computation of the flow in scroll sides

At the inlets of the scroll sides, constant values are prescribed for all variables. The inlet velocities of the turbine and compressor sides of the scroll are prescribed as 67 and 66 $m\,s^{-1}$ respectively, while the corresponding densities are 0·73 and 0·71 $kg\,m^{-3}$. This leads to nearly a 4% difference in the mass flow rates of the two sides. Inlet values for turbulence quantities are derived assuming a 4% turbulence intensity and a mixing length equal to 10% of the inlet radius. Computations are carried out assuming an incompressible flow on the scroll sides.

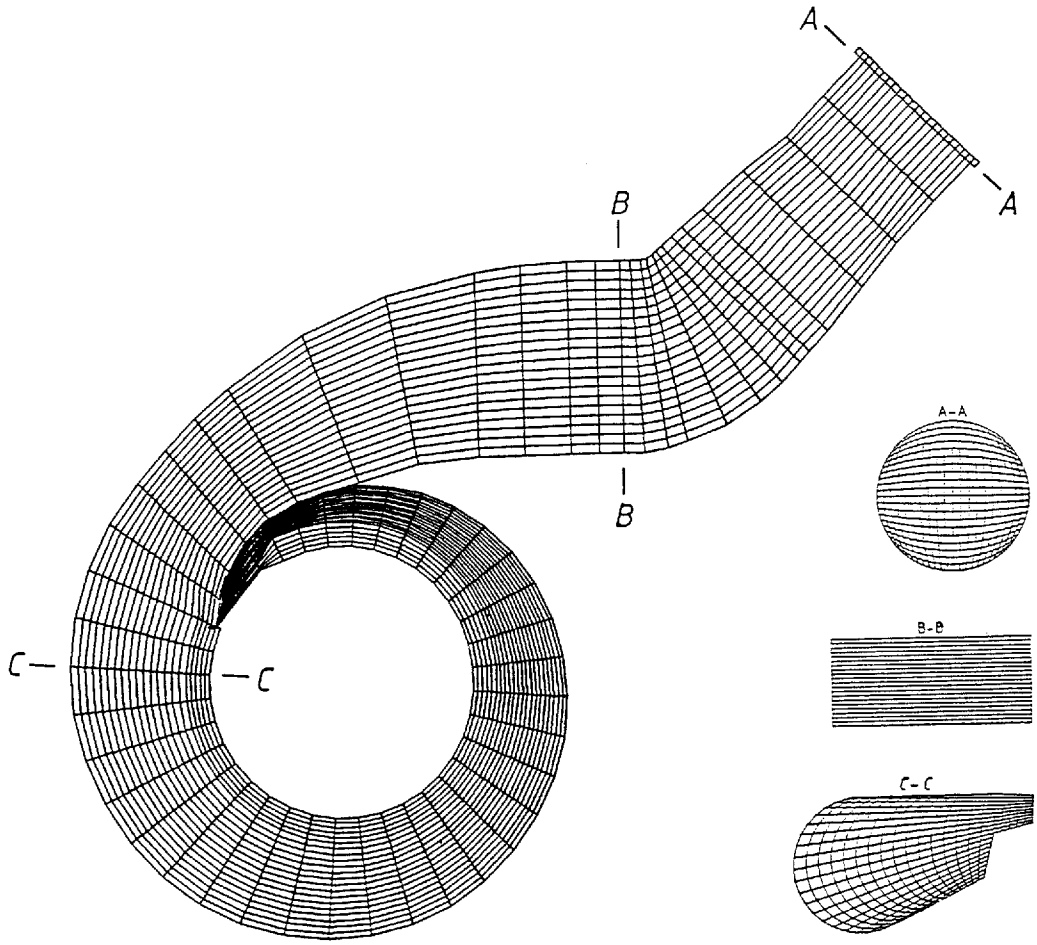

Figure 2. Several sections of 3D grid for TS

Projections of the velocity vectors along several sections are plotted in Figure 4 for the TS and CS. It can be recognized that the flow accelerates along the scroll length, the largest velocities for each cross-section being achieved at the scroll outlet owing to the contraction of the flow area. Furthermore, it is observed that the circumferential velocity components at the outlet are much larger than the normal velocities (Figure 4).

Computation of the flow in the rotor channel

Inlet values for the rotor channel are obtained from the computed results for the scroll sides. For each variable, values are averaged along the circumferential direction for each cell row at the scroll outlets (not at the outlets of the extended solution domains but at the original scroll outlets, as already explained in previous sections; see also Figures 2 and 4). This averaging means of course that the eventual unsteadiness of the flow relative to the rotor due to circumferential non-uniformities of inflow conditions is neglected. Computations are performed for compressible flow in a rotating frame of reference with a given rotor rotational speed of $572\ s^{-1}$.

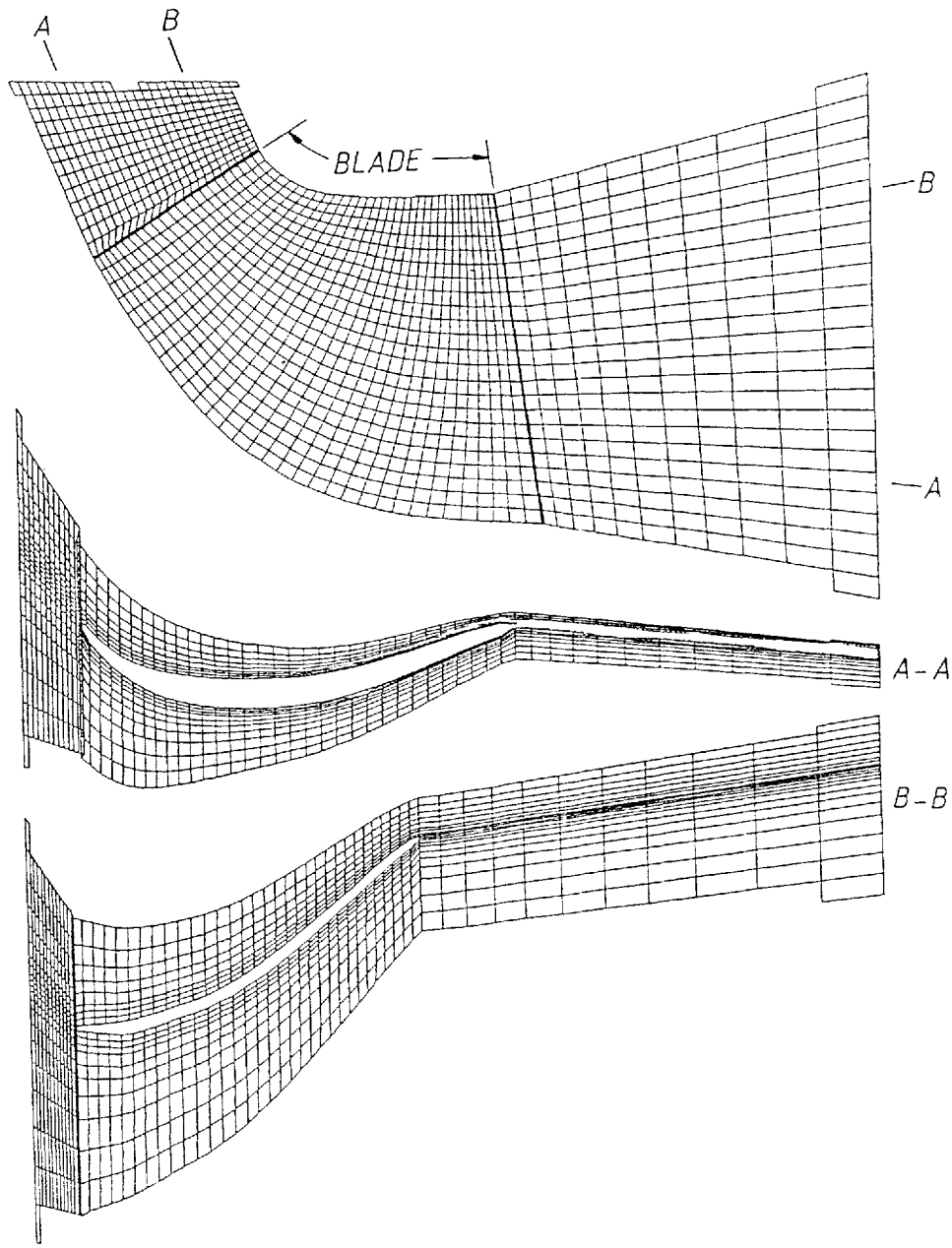

Figure 3. Several sections of 3D grid for RC

Plots of the velocity field obtained for several meridional and blade-to-blade sections are presented in Figure 5. These are projections of curved surfaces along certain grid lines onto constant circumferential angle or constant radius planes, whereas the velocity scale may vary from figure to figure. Looking at the meridional section through the mid-channel, a rather parallel flow can be observed with a low-velocity region near the hub at the mid-span. Deviations

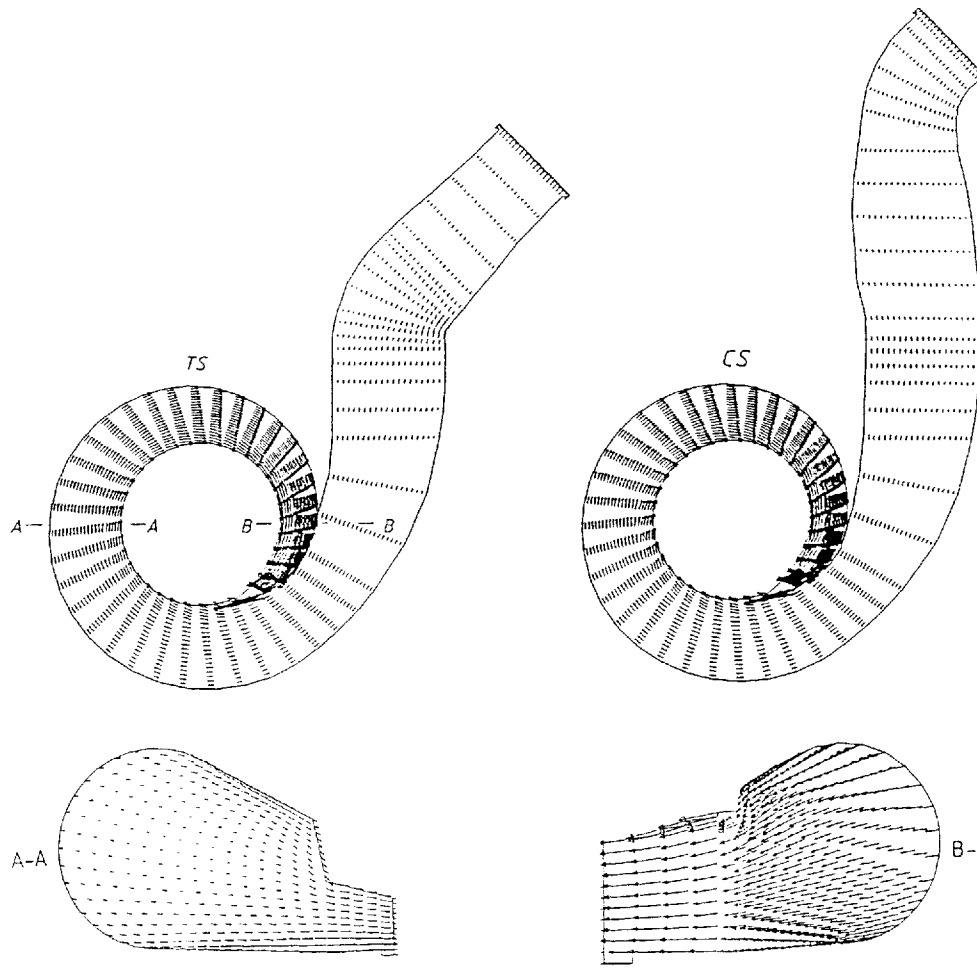

Figure 4. Projections of velocity field on several sections for scroll

from parallel flow are larger at the meridional sections near the suction and pressure sides (Figure 5). This behaviour of the velocity field shows good qualitative agreement with the published results of Dawes[17] for another type of radial turbine. A comparison with in-house measurements has shown that for several important parameters characterizing turbocharger flows the predictions agree with measured values to within 20% tolerance, indicating, in our opinion, an acceptable degree of accuracy for present purposes.

COMPUTATION OF PARTICLE TRAJECTORIES

Computations are carried out for various particle size classes. In the present study, results will be presented mainly for three size classes with diameters 20, 50 and 120 μm. The particle density is assumed to be 2650 $kg\,m^{-3}$.

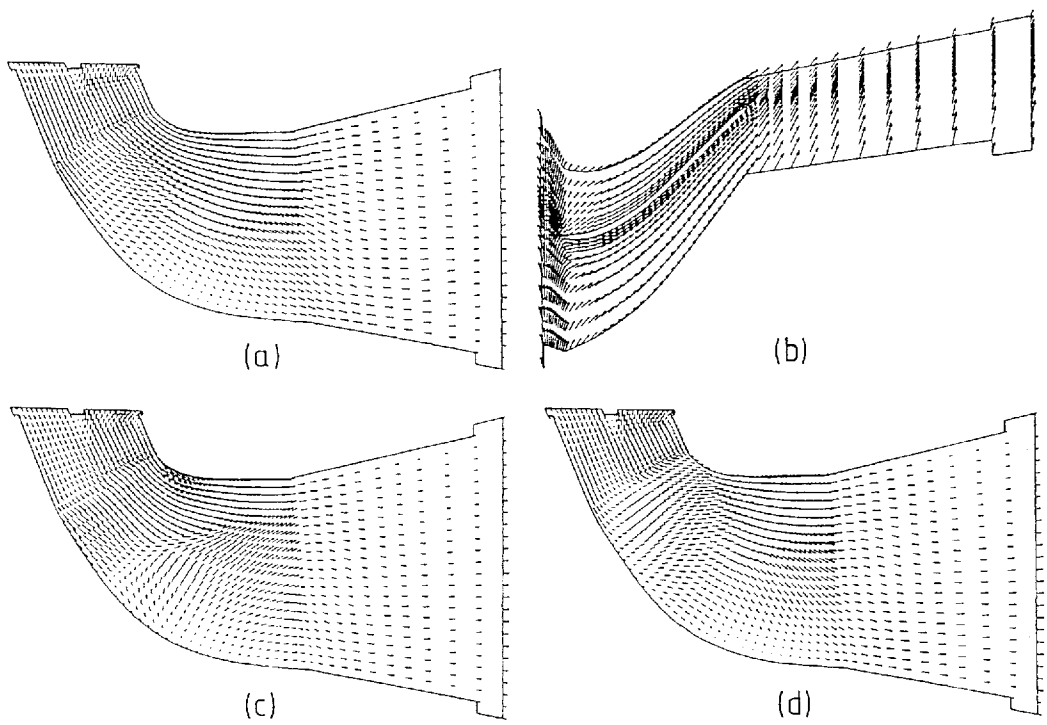

Figure 5. Projections of velocity field on several sections for RC: (a) meridional section at mid-channel; (b) blade-to-blade section near casing; (c) meridional section near suction side; (d) meridional section near pressure side

First, the particle trajectories are computed on both scroll sides for particles injected at the scroll inlets. Subsequently, these particles are followed in the rotor channel. It has been observed that particles are thrown back into the scroll by the rotor. The trajectories of thrown-back particles are subsequently followed again on both scroll sides until they leave the scroll again. As also indicated by experiments, the throw-back of particles repeats itself many times. Here only one throw-back step is considered.

In the following, the particles in the scroll which come directly from the scroll inlet will be denoted as first-pass particles, while the particles which are thrown back into the scroll will be denoted as re-entering particles.

Computation of particle trajectories for first-pass particles

At scroll inlets, particle velocities are assumed to be equal to the local gas velocity. For each size class, 100 particles are followed for each scroll side. A uniform distribution of particles is assumed at scroll inlets.

In Figure 6 the trajectory of a 20 μm particle on the TS is shown, where the grid is indicated using a reduced number of grid lines for clarity. After making its first impact, the particle is immediately caught by the centrifugal force and pushed towards the outer wall in the rolling part of the scroll. It cannot leave the outer scroll wall until it reaches the scroll end, having many impacts with the scroll wall on its way (Figure 6). This behaviour is qualitatively the same for all particles of all three size classes on both scroll sides. However, it has been observed for smaller

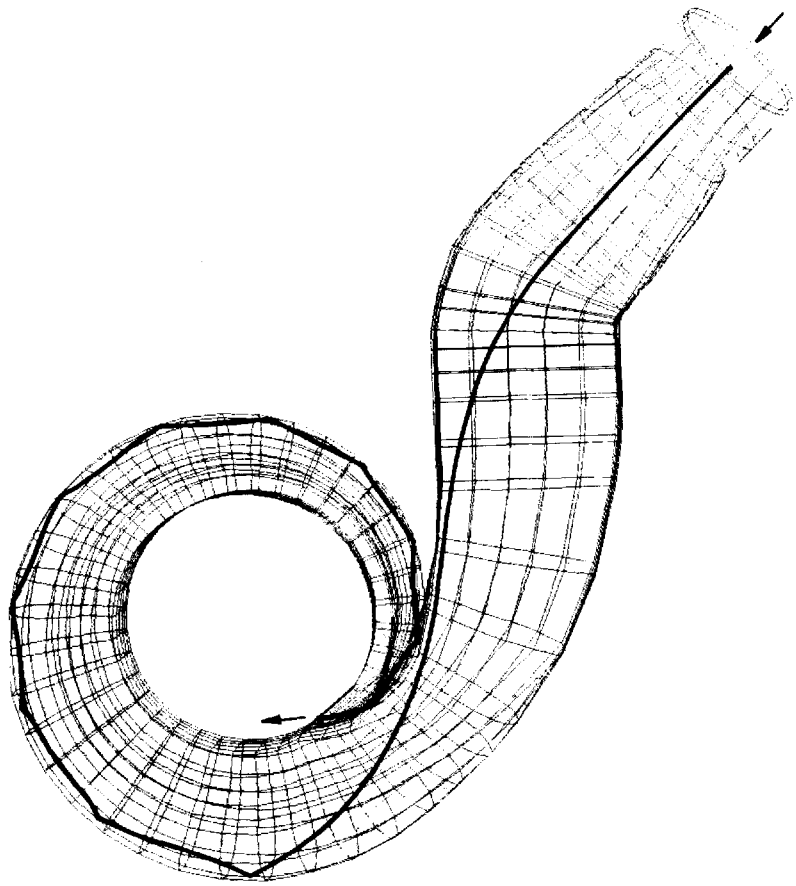

Figure 6. Trajectory of a 20 μm particle in TS (first pass)

size classes ($d_P \leqslant 10$ μm) that particles do not necessarily show this behaviour and may go into the rotor channel, following the gas flow, before the scroll end is reached, which is an expected behaviour.

Computation of particle trajectories in the rotor channel

Derivation of the inlet conditions. In the computation of particle trajectories in the rotor channel, the particle data at the scroll outlet obtained from the scroll computations are used in deriving the inlet conditions for the rotor channel. However, since it would be quite a difficult task to follow each individual particle (the relative blade position is also uncertain), the data had to be brought into a useful form by averaging as described below.

Locations of injection points. Eight equidistant injection locations are prescribed in the circumferential direction at the inlet of the considered rotor channel sector. For the axial direction (rotor co-ordinate system, Figure 1), three equidistant injection points are assumed.

Spatial inlet distributions. In the circumferential direction a uniform distribution is assumed. In the axial direction (rotor co-ordinate system, Figure 1), local distributions of particles given by

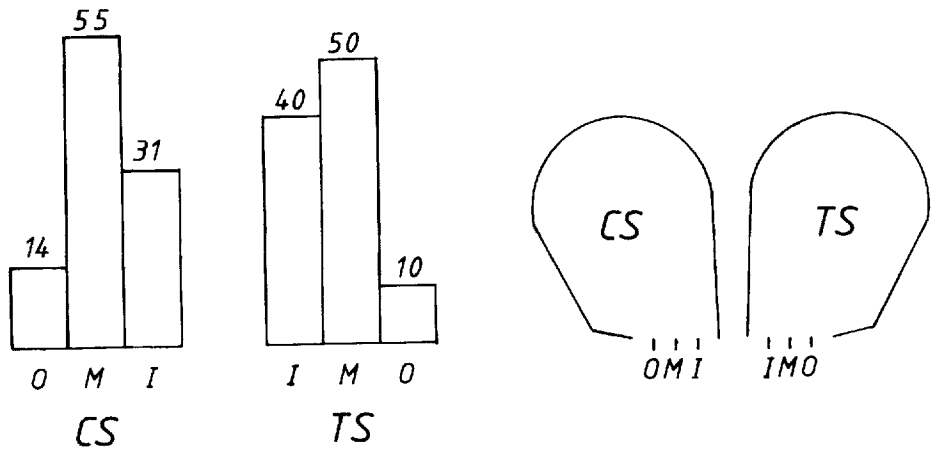

Figure 7. Distribution of occurrence frequencies between axial injection locations at scroll outlet for 120 μm particles (first pass)

the scroll results are taken into account separately for each size class and scroll side. Figure 7 shows the distribution of averaged occurrence frequencies of 100 particles at three axial injection locations for the particle size class 120 μm for both scroll sides. The particle concentration is maximum in the middle location for both scroll sides, whereas the concentrations at the outer locations (on the sudden contraction side) are minimum. This behaviour is observed qualitatively for all size classes and both scroll sides.

Inlet velocity distributions. It has been thought to be a rough assumption to represent each velocity component by a single mean value for each scroll side.

For the axial velocity component (rotor co-ordinate system), which has quite small values compared with the radial and circumferential ones, a single mean value is used for each scroll side.

In defining the representative radial and circumferential velocities, their correlation is also investigated to avoid specifying too many velocity classes. Figure 8 illustrates the occurrence frequencies of 100 particles in the two-dimensional space spanned by the radial and circumferential velocity components for $d_P = 20$ μm and the TS (velocities in the stationary frame of reference). Here a certain pattern of correlation between the radial and circumferential velocities can be recognized. The non-zero terms of the matrix form a diagonal extending from the high-$|v_P|$–low-$|w_P|$ to the high-$|w_P|$–low-$|v_P|$ corner. The low-$|v_P|$–low$|w_P|$ and high-$|v_P|$–high-$|w_P|$ corners are empty, indicating that particles with low radial and circumferential velocities or high radial and circumferential velocities do not occur (magnitudes of velocities are referred to as high and low). Similar distributions are observed for all size classes at the outlets of both sides.

Using the information sketched in Figure 8, the particle velocities at the inlet of the rotor channel are represented by three velocity classes for each particle size class and scroll side. The diagonal shown in Figure 8 is divided into three representative parts, namely the two corners and the middle part. (Divisions are determined in an *ad hoc* manner by assuming that dividing lines pass through mid-locations between mean and minimum/maximum velocity values.) Subsequently, average values for velocities are obtained separately for each of the three parts, namely for the high-$|v_P|$–low-$|w_P|$ region (part I, Figure 8), the medium-$|v_P|$–medium-$|w_P|$ region (part II) and the high-$|w_P|$–low-$|v_P|$ region (part III). Thus the distribution in the velocity space at the inlet of the rotor channel is represented by three velocity classes, each having one of the averaged pairs

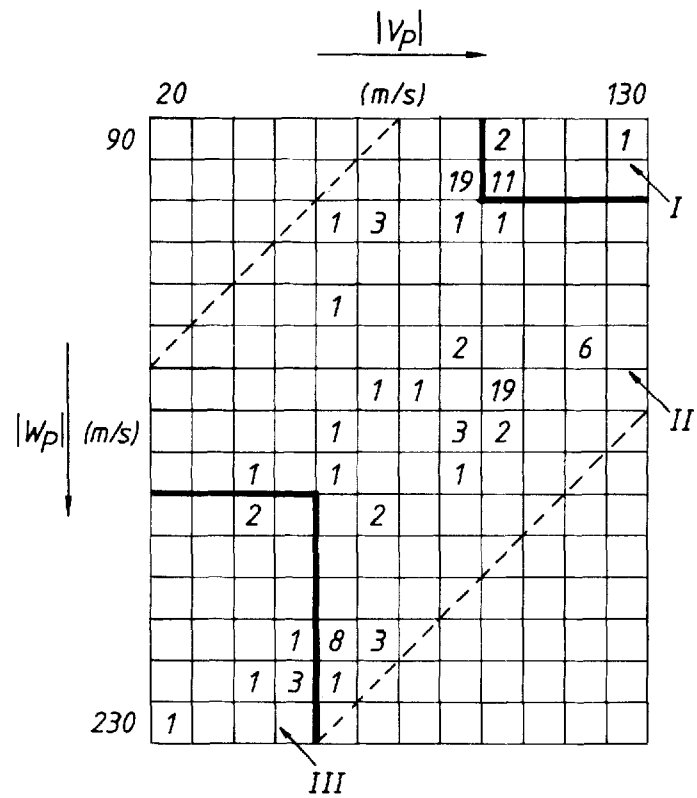

Figure 8. Occurrence frequencies in two-dimensional velocity space spanned by radial and circumferential velocities at TS outlet for 20 μm particles (first pass)

of values for the three velocity regions as indicated in Figure 8, for each size class and scroll side. In the following, the expressions high-$|v_P|$–low-$|w_P|$, medium-$|v_P|$–medium-$|w_P|$ and high-$|w_P|$–low-$|v_P|$ will be shortened to high-v, medium and high-w respectively for simplicity.

The number of injection points for each scroll side is chosen to be 24. Since the velocity distribution is represented by three velocity classes, three particles are injected at each injection point, resulting in 72 particles coming for each scroll side. Each of these particles is correlated with the 100 particles coming from one scroll side, using the above-mentioned distributions in velocity and space, letting each particle starting at the rotor channel inlet represent a certain percentage of particles coming from the scroll depending on its injection location and velocity class. In other words, the percentage (P_{IJK}) of particles coming from a scroll side represented by a particle starting at the rotor channel inlet at the Ith circumferential and Jth axial locations and belonging to the Kth velocity class is approximated as

$$P_{IJK}=P_I P_J P_K, \tag{13}$$

where

$$\sum_{K=1}^{3}\sum_{J=1}^{3}\sum_{I=1}^{8} P_{IJK}=1. \tag{14}$$

In (13) and (14), P_I, P_J and P_K are obtained from the above-mentioned spatial (P_I, P_J) and velocity (P_K) distributions. P_I is always equal to $\frac{1}{8}$, since a uniform distribution is assumed in the circumferential direction. Speaking for Figure 7, for example, P_J is equal to 0·50 for a particle starting at the mid point of the TS. Considering the distribution in Figure 8, P_K is equal to 0·14 for a particle belonging to high-v velocity class.

Results. Figure 9 shows the 3D representation of a particle trajectory in the rotor channel.

The domain illustrated in Figure 9 is the circumferential sector of the rotor channel considered in computations. Periodic boundary surfaces bounding the domain in the circumferential direction are not shown in the figure. Only the exit and re-entry points of the particle through these boundaries are indicated by the numbers 1 and 2. Figure 9 may look a little confusing at first sight owing to discontinuities of the particle path at periodic boundaries. This is due to the fact that the path of the particle, which travels through three adjacent sectors, is computed and drawn using the single sector under consideration. (Flow fields of all sectors are assumed to be identical.) When the particle leaves the current sector through a periodic boundary (the right-hand-side boundary in Figure 9), the continuation of the path in the next sector is computed again using the same sector by injecting the particle through the periodic boundary on the opposite side (left-hand side in Figure 9) at the corresponding location. This occurs twice for the particle path illustrated in Figure 9, i.e. the particle 'sees' in reality three adjacent sectors.

The particle in Figure 9 is injected from the TS of the scroll. Penetrating the rotor channel while simultaneously moving in the circumferential direction, it enters the adjacent sector by crossing the periodic boundary (points 1 in Figure 9). Under the influence of the centrifugal force it then starts to move radially outwards. On impact with the lip separating the TS and CS, it starts to move radially inwards again. After passing through the periodic boundary for the second time, i.e. entering the third circumferential sector (points 2 in Figure 9), it starts to move radially outwards. After a few more impacts with the lip it leaves the rotor channel and turns back into the TS.

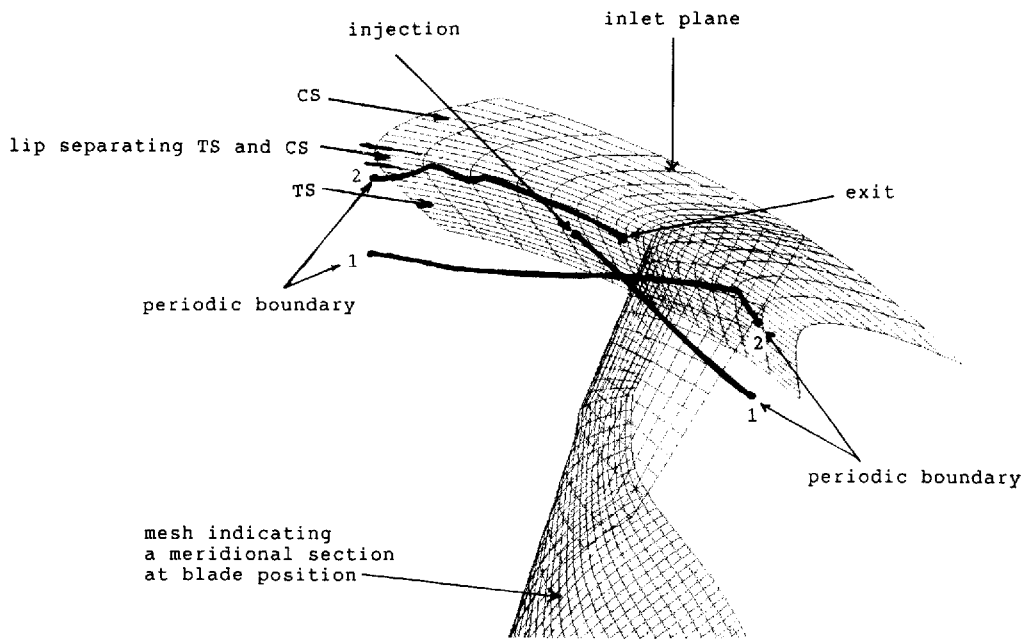

Figure 9. 3D representation of a particle trajectory in RC

The important results can be summarized as follows.

(a) Particles coming from the scroll are thrown back at very high rates. Actually, no particle has managed to pass through the RC without getting thrown back into the scroll. This point will be further discussed below.

(b) The main throw-back mechanism does not require a physical contact with the blade. The majority of particles are thrown back solely under the influence of the centrifugal force field owing to their own rotational motion. The strength of this field was already demonstrated when inspecting first-pass particles in the scroll (Figure 6), where particles were strongly pressed against the outer scroll wall.

In Table I the numbers of particles hitting the blade are given for particles coming from both scroll sides and for three size classes. These numbers are converted accordingly for 100 particles coming from each scroll side (equations (13) and (14)).

One can see in Table I the general tendency that the number of particles hitting the blade increases with increasing particle size. This is an issue related to the differing inlet velocities, as will be mentioned below. Particles strike the blade on the suction side since they have velocities lower than the blade velocity.

To estimate the effect of an impact with the blade for the erosion of the scroll by re-entering particles, two particles of the same size class are compared. The particles have the same inlet velocities and move into the RC at nearly the same depth. The first one turns back after making an impact with the blade, whereas the second one turns back without an impact. At the scroll outlet, as the particles re-enter the scroll, the first particle turns out to have a speed 45% higher than the second one. This comparison shows that particles having contact with the blade re-enter the scroll at higher speeds than particles that do not strike the blade. Therefore particles having contact with the blade are more erosive for scroll parts. However, since, according to the present model, the majority of particles re-enter the scroll without striking the blade (Table I), the re-entry velocities in the mean are not too high.

In Figure 10, boundaries of the struck regions on the blade are indicated. (Struck regions do not necessarily have rectangular shapes. Black areas indicate the boundaries of a rectangular region enclosing the struck region.) One sees that impacts occur near the leading edge. An impact with the blade increases the circumferential velocity of the particle (in the stationary frame of reference) and contributes to its turning back. Another mechanism supporting the throw-back of particles by impacts is the blade curvature near the leading edge, since the particles make their impacts very close to the leading edge and approach the leading edge at very flat angles.

(c) There is a large flux of particles from the CS of the scroll to the TS. The particles coming from the CS go into the TS at high rates as they get thrown back. There is no flux in the reverse direction. Table II gives the numbers of particles moving from one scroll side into the other.

Figure 11 illustrates computed trajectories for two particles injected from the CS and TS. The particle coming from the CS goes back into the TS after hitting the lip. The particle coming from the TS turns into the TS again. The lip is under serious threat of erosion damage, since it is struck by substantial numbers of particles (nearly 40% of particles from the CS and 10% from the TS).

The predicted behaviour of particle trajectories agrees quite well with many practical observations. For example, in an in-house experimental study the erosive particles were injected only at the inlet of the CS whereas the gas flowing into the TS was particle-free. In this case it has been observed that after a certain time the TS was eroded even more strongly than the CS. This observation confirms that the particles are thrown back into the scroll and that substantial numbers of particles coming from the CS go into the TS as they are thrown back. It also shows that the erosion is strongly influenced by the thrown-back particles.

Table I. Numbers of particles hitting the blade

	20 μm	50 μm	120 μm
CS	0	1	11
TS	1	23	25

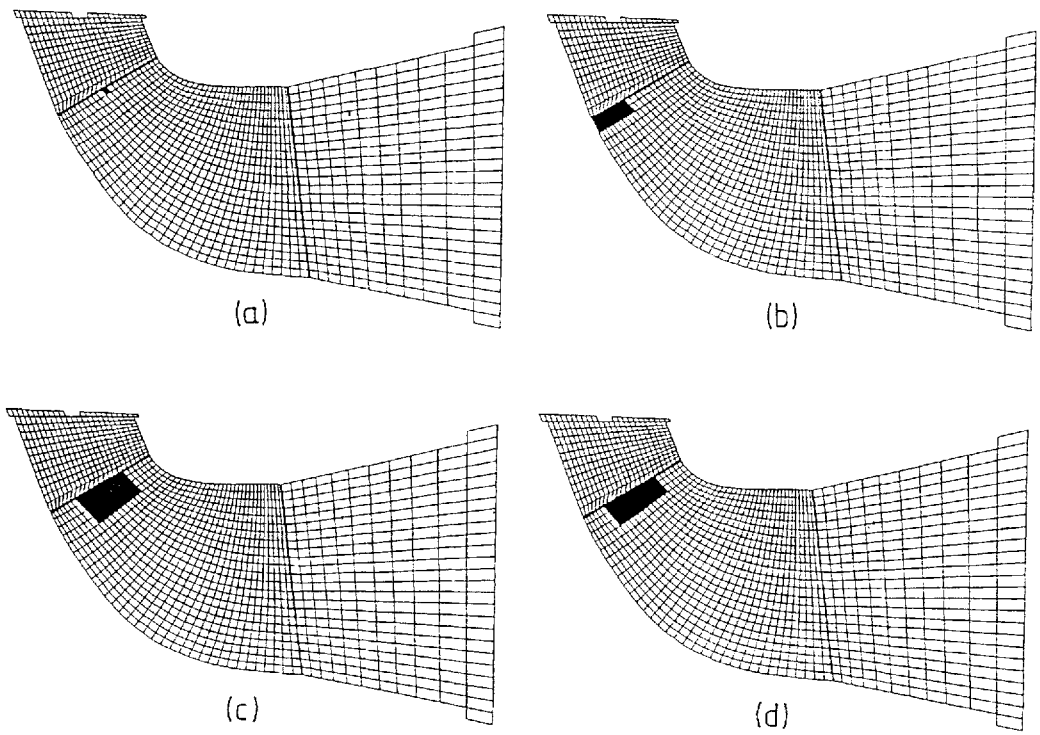

Figure 10. Boundaries of struck regions on rotor blade: (a) CS, 50 μm; (b) CS, 120 μm; (c) TS, 50 μm; (d) TS, 120 μm

Table II. Numbers of particles exchanged between scroll sides

	20 μm	50 μm	120 μm
CS→TS	47	36	82
TS→CS	0	0	0

(d) As already mentioned at the beginning of this section, all particles belonging to the three considered size classes are thrown back into the scroll. This cannot reflect the real situation, since in this case a continuous accumulation of these size classes would take place in the scroll, which does not agree with practical observations.

On the other hand, one can also argue that these particles may manage to pass through the RC after several throw-back steps, since at each step the inlet conditions to the RC and the whole flow situation may change owing to several reasons. Here the most important reason is the growing

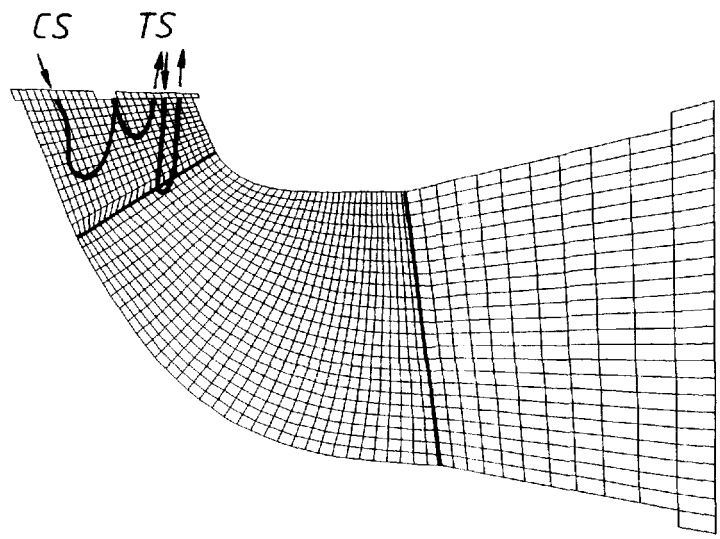

Figure 11. Two typical particle trajectories in RC starting from CS and TS outlets

particle–gas and particle–particle interactions due to the continuous accumulation of these particles. This phenomenon could not be investigated, since these interactions were neglected in the present model.

Nevertheless, the through-flow behaviour of particles in the RC is investigated here a little further within the framework of the present modelling assumptions, as described below.

An investigation of particle paths shows that there is a common rule about the penetration depth of particles into the RC. The distance a particle penetrates into the RC (before it starts to turn back into the scroll) increases in proportional to the ratio $|v_p/w_p|$ at the RC inlet (velocities in the stationary frame of reference). For the three inlet velocity classes assumed, the particles with the highest $|v_p/w_p|$-ratios are those belonging to the high-v class (Figure 8). Consequently, for each size class, these are the ones which manage to penetrate the maximum distances into the RC compared with the other velocity classes. However, the high-v class values are still averaged values for several particles belonging to this class (Figure 8). Therefore the average high-v velocities still give lower $|v_p/w_p|$-values than the maximum $|v_p/w_p|$-values occurring for some individual particles. One can expect that these individual particles with the maximum $|v_p/w_p|$-ratio, i.e. particles with the upper right corner velocity pair of the velocity diagonal shown in Figure 8, have the highest chance of passing through the channel (speaking for Figure 8, the particle with velocities $|v_p| = 130$ m s^{-1}, and $|w_p| = 90$ m s^{-1}). The present resolution of the RC inlet values into three classes was, however, not fine enough to capture this velocity pair.

Therefore a study is carried out by specifying the individual particle velocities giving the maximum $|v_p/w_p|$-ratio (the upper right velocity pairs of diagonals such as that in Figure 8) as inlet conditions for all injected particles into the RC, while keeping the number of particles and their injection locations as before. The investigation is carried out for three particle size classes, but only for particles coming from the TS, since particles managing to pass through the RC are more likely coming from the TS (Table II, Figure 11).

Furthermore, the effect of turbulence on the inlet conditions is also investigated using simplifying assumptions. The fluctuational components of the gas velocity at the RC inlet are estimated

from the turbulence kinetic energy, assuming isotropic turbulence. It is further assumed that these fluctuations are perfectly followed by particles at the RC inlet. Thus the fluctuational values are added to the particle inlet velocities of the previous step in such a way that the maximum $|v_p/w_p|$-value is further increased (i.e. v_p is increased and w_p is decreased in magnitude by the amount of the fluctuational velocity). In this case the axial velocity component (u_p) is also increased by the amount of the fluctuational value. This modification holds only for inlet velocities, of course. Trajectories in the solution domain are computed neglecting turbulent fluctuations as before. This study has been performed only for 20 μm particles for comparison purposes.

The numbers of particles managing to pass through the RC, using maximum $|v_p/w_p|$-values as inlet conditions (for 20, 50 and 120 μm particles) and using the additional turbulence modification of these inlet values (only for 20 μm particles), are listed in Table III. It can be seen from Table III that some particles passing through the RC can now be identified using inlet velocities with maximum $|v_p/w_p|$-ratio. Such particles belong to the 50 and 120 μm classes, whereas 20 μm particles still do not manage to pass through the RC under this inlet condition. For 20 μm particles one can observe, however, that the additional 'turbulence modification' of the inlet velocities leads to a substantial number of such particles being identified.

Particles represented by these special inlet velocity classes are much fewer, of course. Conclusively, one can say that (1) the flow rate of particles through the RC is very small and (2) this small through-flow rate is quite sensitive to inlet conditions.

Figure 12 illustrates the trajectory of a 20 μm particle passing through the RC. Trajectories of all particles passing through the RC show the same qualitative behaviour. These particles also start to move radially outwards under the influence of the centrifugal force after a certain penetration depth is reached, as observed for all other particles (Figures 9 and 11). The decisive point for a particle to pass through the channel seems to be the location at which it lands on the casing wall as it moves radially outwards. If the particle has moved deeply enough in the axial direction, it reaches the casing wall at a location where the inclination of the casing wall is very flat. In this case the centrifugal force cannot push the particle any further and the particle can be captured by the flow in the axial direction.

Computation of particle trajectories for re-entering particles

Inlet velocities for particles re-entering the scroll are obtained by averaging the results obtained by the RC solution. For a certain size class and scroll side, only a single global average value is used for each velocity component.

Re-entry locations of particles are not very easy to compute (uncertain relative blade position of particles entering the channel, modification of residence times by turbulence). Therefore a detailed estimation of re-entry locations is not attempted. Instead, two extreme cases are considered between which the reality can be assumed to lie.

Table III. Numbers of particles starting from the TS and passing through the RC under certain inlet conditions

	20 μm	50 μm	120 μm
max $\lvert v_p/w_p \rvert$	0	33	4
max $\lvert v_p/w_p \rvert$ + turbulence modification	38	--	-

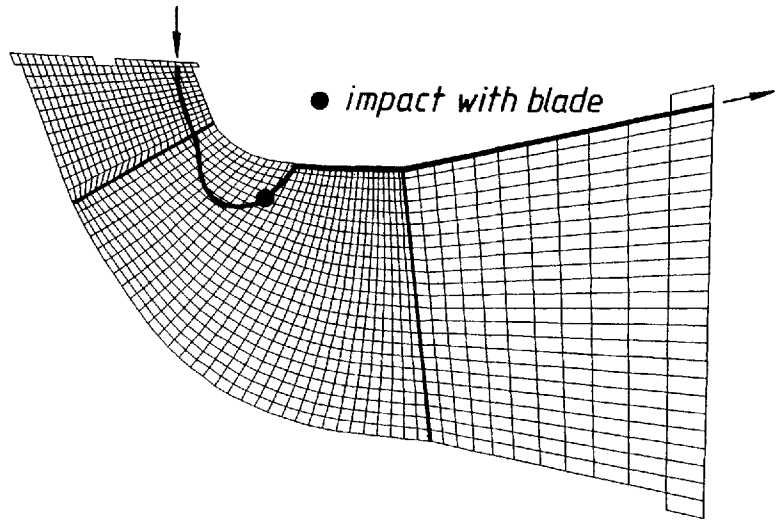

Figure 12. A 20 μm particle passing through RC

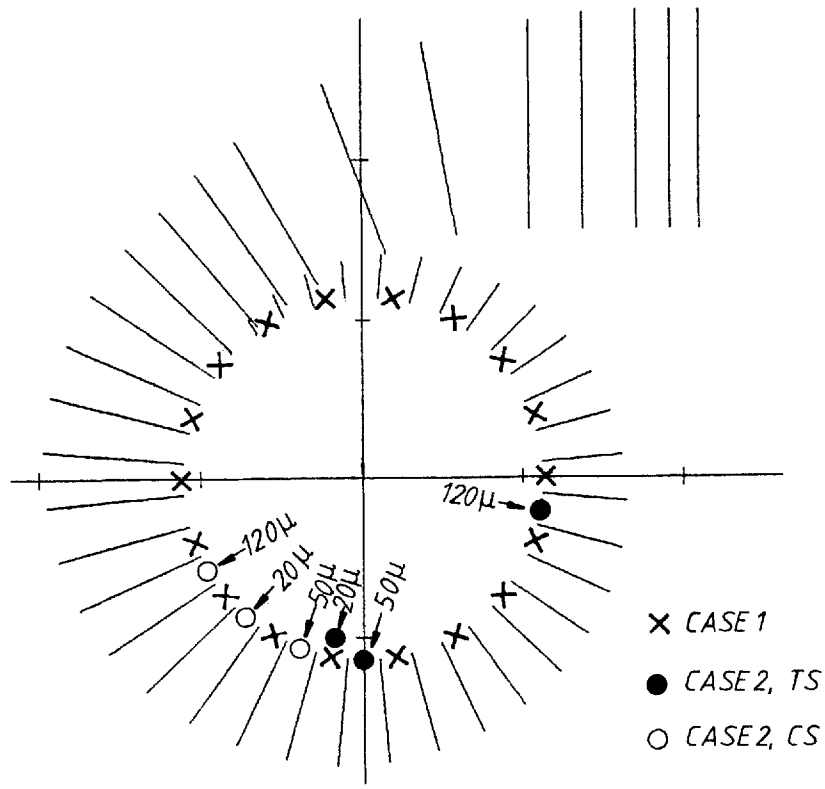

Figure 13. Circumferential injection locations for re-entering particles for cases 1 and 2

In the first case (case 1), particles are assumed to re-enter the scroll with a uniform distribution along the circumference. In the second case (case 2), single circumferential re-entry locations are defined for each particle size, which differ from scroll side to scroll side. These points are determined using an average residence time for particles in the RC (different for each size class and for each scroll side) and assuming all particles enter and leave the RC at the same position relative to the rotor blade. A uniform axial distribution is assumed. These injection locations are

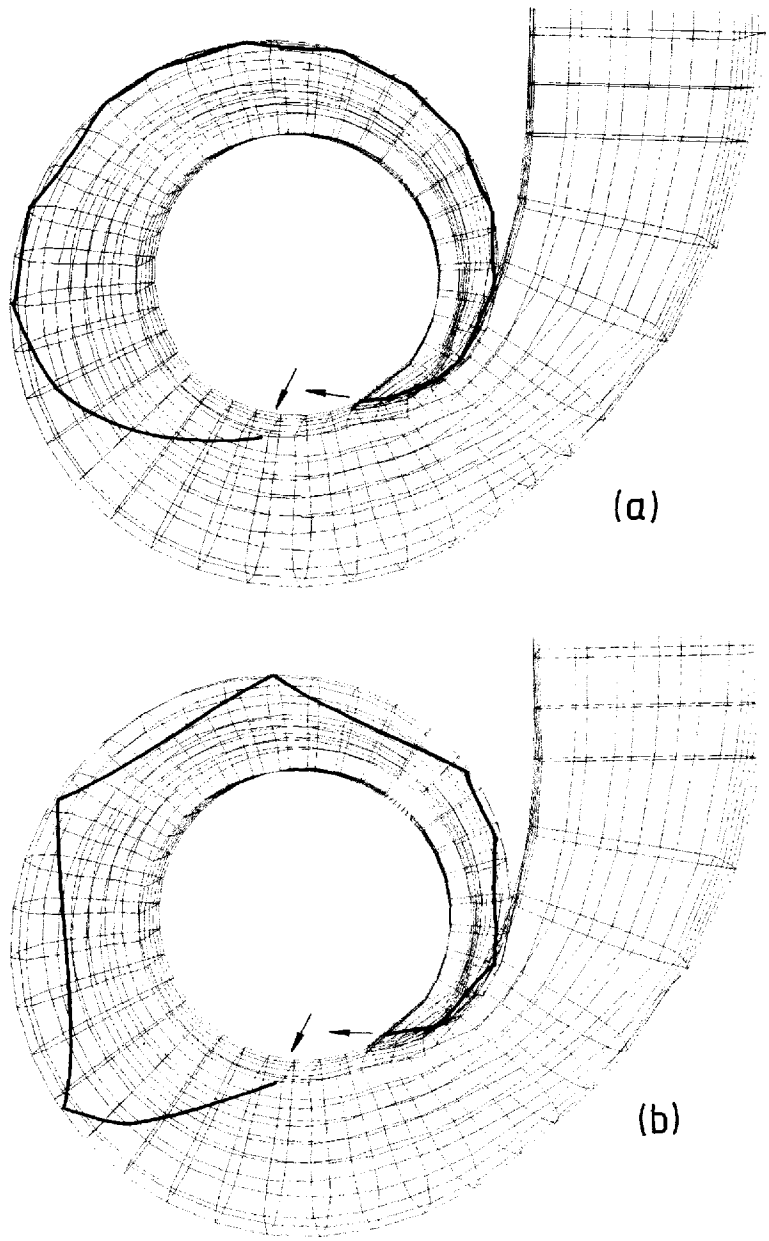

Figure 14. Trajectories of re-entering particles in TS: (a) 20 μm; (b) 120 μm

shown in Figure 13. Since particles re-entering the TS also contain particles coming from the CS (travelling larger distances, Figure 11), their average residence times in the RC are larger than those of particles re-entering the CS. This causes TS re-entry locations to be generally located further downstream. The movement of particles from the CS to the TS is extremely high for 120 μm particles (Table II). For this size class, practically all particles belonging to the high-v and medium inlet velocity classes (Figure 8) move to the TS. The remaining particles belonging the high-w inlet velocity class have the smallest chance of penetrating the RC and thus are thrown back quite quickly. This causes the CS re-entry point for 120 μm particles be located somewhat upstream (Figure 13).

Figure 14 shows trajectories of two re-entering particles for size classes 20 and 120 μm. Larger particles make greater jumps along the scroll wall. A certain similarity between the paths of re-entering (Figure 14) and first-pass (Figure 6) particles can be observed, since they all follow the outer scroll wall and go into the RC at the scroll end.

A further comparison of first-pass and re-entering particles shows that their outlet velocities are also similar. Deviations of averaged values are below 10% for speeds and below 1% for directions, indicating a slow change in scroll outlet conditions from one throw-back step to another under the present modelling assumptions.

COMPUTATION OF THE EROSION DAMAGE

In the following, the results will be presented consistently with the assumed inlet particle load of 100 particles per scroll side, considering the particle exchange between scroll sides as they re-enter the scroll.

Erosion damage in the scroll caused by first-pass particles

Figure 15 shows the distribution of impact frequency along the scroll wall in the TS, for the ninth section counted from the scroll end, for 20 μm particles. One can see that impacts occur within a small region near the largest radial position, since particles are forced to concentrate there by the centrifugal force.

The variation in the erosion damage along the scroll length is illustrated in Figure 16 for 120 μm particles and the TS. In this representation each column denotes the erosion damage at a cross-section along the scroll length (by 'cross-section', a slice of computational cells is meant). These numbers are obtained by summing the erosion damage along the periphery (Figure 15) of each cross-section. Irregularities in the distributions are due to the representation of the particle phase with a moderate number of particles, not sufficing yet to produce smooth data. This qualitative behaviour is the same for all size classes and both scroll sides. The erosion damage increases steeply along the scroll, achieving maximum values at the scroll end. This is due to

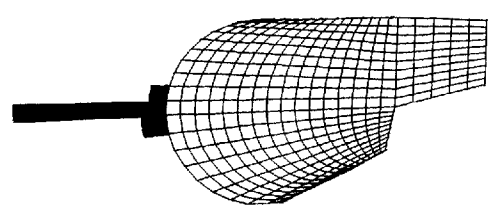

Figure 15. Distribution of impact frequencies for scroll cross-section

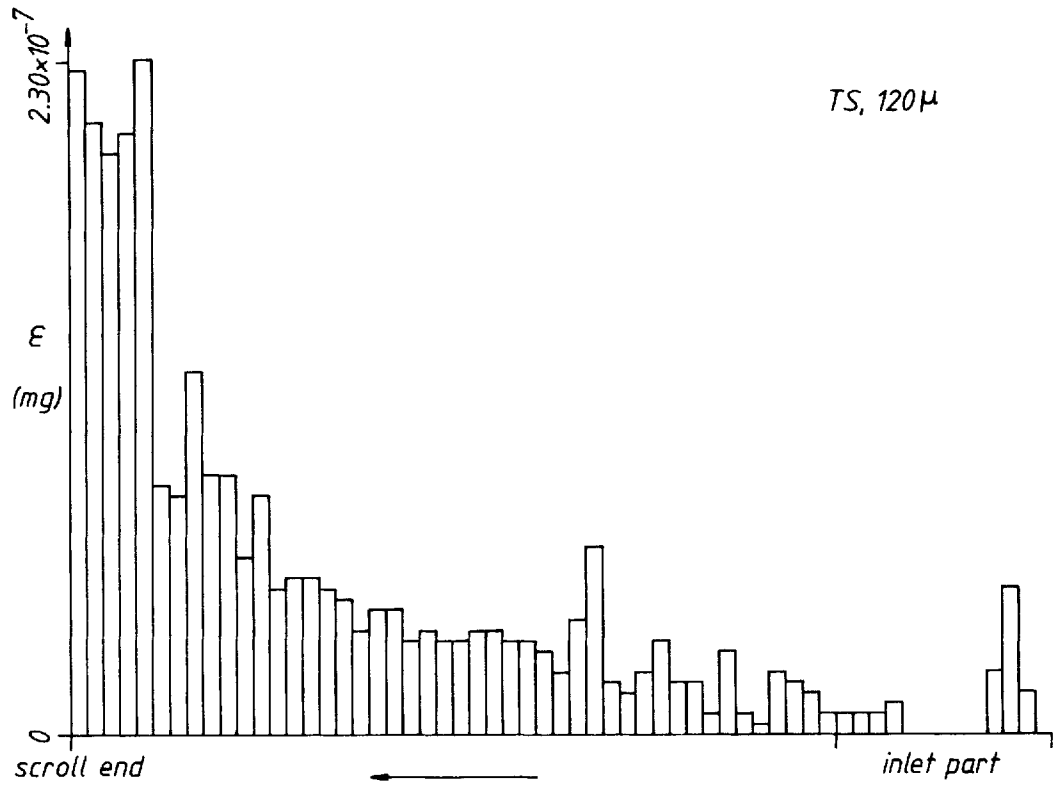

Figure 16. Variation in erosion damage along scroll length for first-pass particles (TS, 120 μm)

increasing fluid velocity along the scroll length (Figure 4). Particles move along the outer scroll wall by making impacts with the wall (Figure 6). After each impact they come into a region with higher fluid velocities which cause them to accelerate. Since the erosion damage depends exponentially on the particle speed (equation (12)), an increase in the particle speed is felt much more strongly in the erosivity. In Figure 16 the expression 'inlet part' indicates the portion of the scroll between the inlet plane and the flange (Figure 1).

The variation in the total erosion damage (obtained by summing the values over all cross-sections, Figure 16) for first-pass particles with varying particle size class is presented in Figure 17 for both scroll sides. One can see that the values are greater for the TS than for the CS. This is due to slightly different mass flow rates through the two scroll sides. The total erosion damage increases with increasing particle size for both scroll sides. This increase in erosion damage with particle size is, however, purely due to the increase in the mass of the particles. Figure 18 shows the 'specific' values, i.e. the erosion damage per mass of injected particles. One observes here the reverse tendencies, since small particles flow with higher speeds than large ones.

Erosion damage in scroll parts caused by re-entering particles

For case 1 the erosion damage along the TS for 120 μm particles is illustrated in Figure 19; a similar tendency is observed in other cases. Here the initial parts of the scroll do not experience

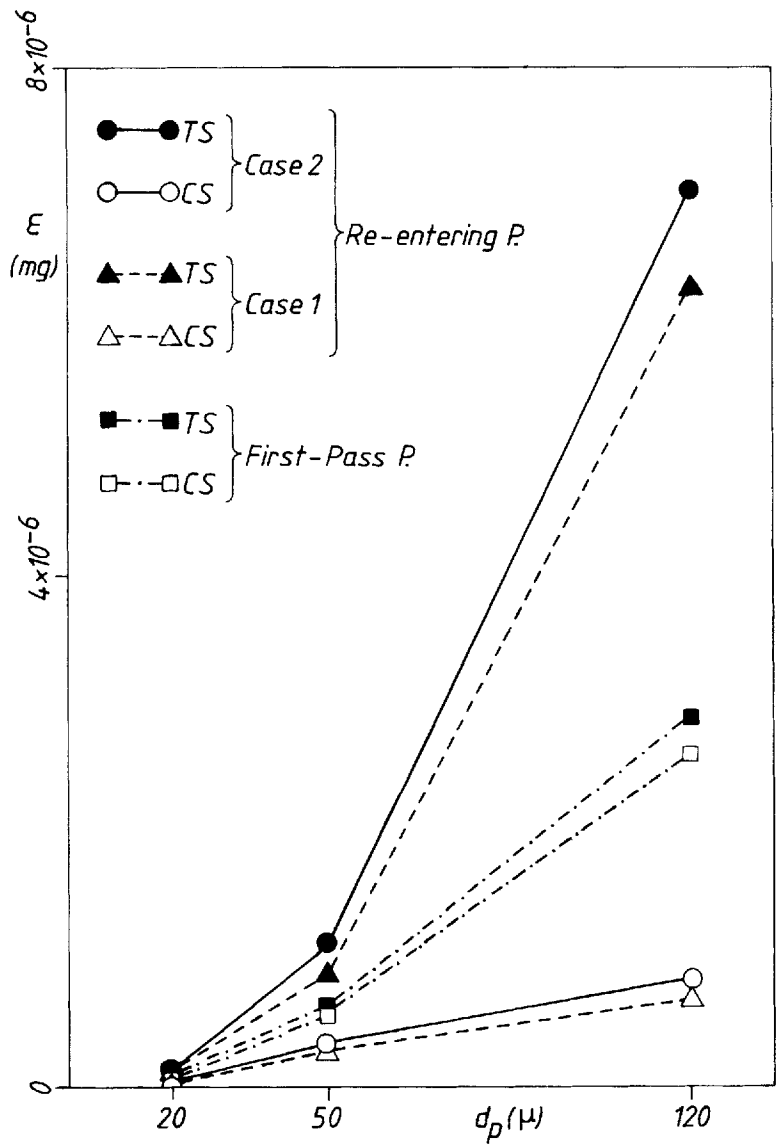

Figure 17. Variation in total erosion damage with particle size class for first-pass and re-entering (cases 1 and 2) particles

any erosion damage, of course. Similar to the results for the first-pass particles, the erosion damage shows here also an increase along the scroll length, reaching its maximum near the scroll end.

In Figure 17 the variation in the total erosion damage with varying particle size class is plotted for both scroll sides for case 1. One can observe that the erosion caused by particles re-entering (case 1) the TS is much larger than that for the CS. This is mainly due to the different numbers of particles re-entering the TS and CS (Table II). The TS curve for re-entering particles is also higher than the TS and CS curves for first-pass particles, whereas the CS curve for re-entering particles shows smaller values than for first-pass particles.

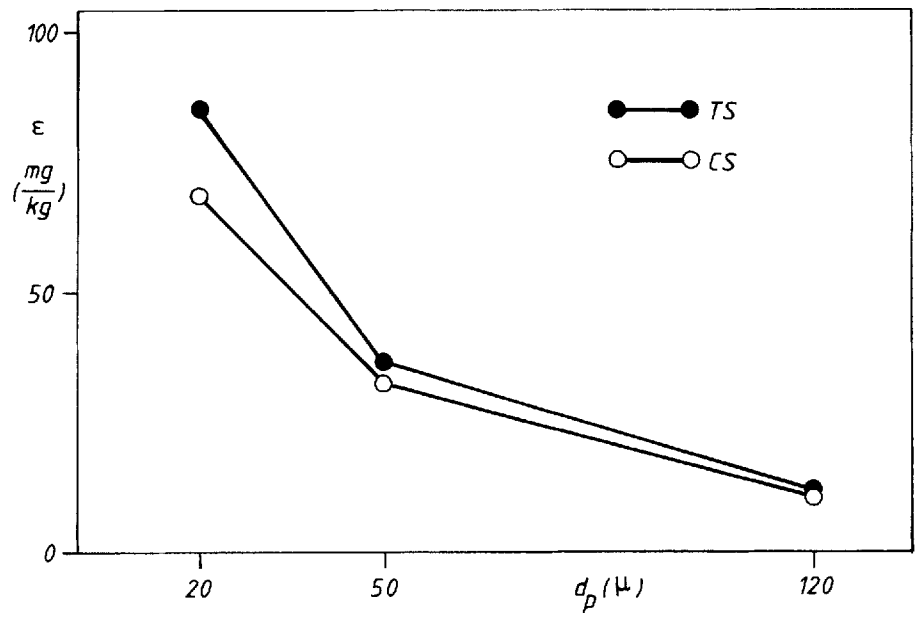

Figure 18. Variation in total erosion damage per mass of injected particles with particle size class for first-pass particles

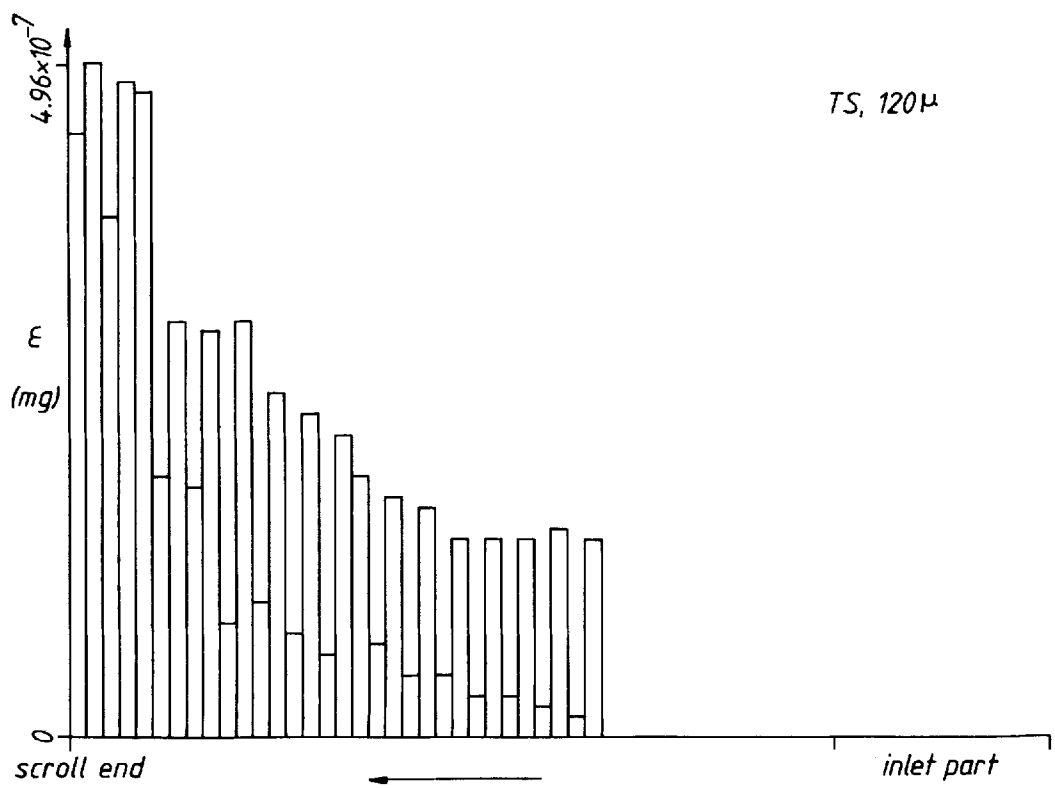

Figure 19. Variation in erosion damage along scroll length for re-entering particles for case 1 (TS, 120 μm)

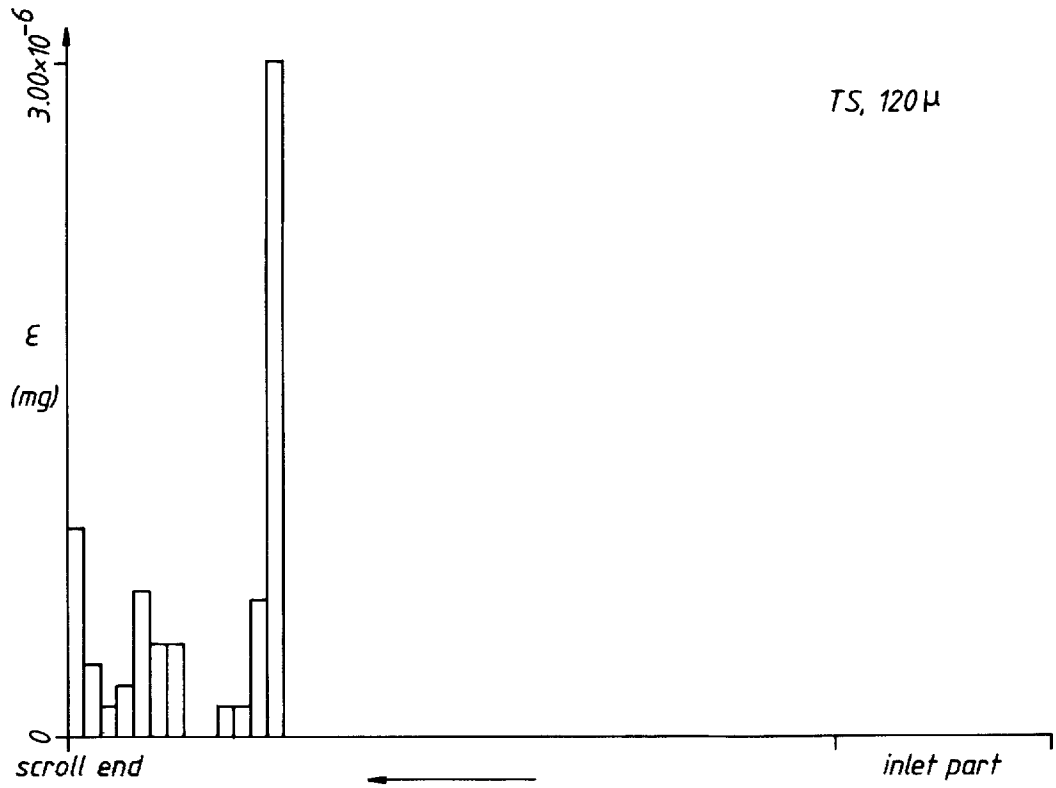

Figure 20. Variation in erosion damage along scroll length for re-entering particles for case 2 (TS, 120 μm)

The variation in the erosion damage along the scroll for case 2 is shown in Figure 20 for 120 μm particles and the TS. The behaviour observed here is quite different from that of Figures 16 and 19. Here maximum erosion values are generally attained at the first impact location of particles instead of at the scroll end. Regions of possible maximum erosion values (depending on particle size) according to the case 2 results are illustrated in Figure 21.

The variation in the total erosion damage with varying particle size class for case 2 is also presented in Figure 17. The case 2 results also show a much larger erosion of the TS than of the CS. A very interesting point here is the similarity of the case 1 and 2 curves (Figure 17). This implies that the total erosion damage is quite insensitive to the distribution of injection points at re-entry.

CONCLUSIONS

The erosion behaviour in the radial turbine of a turbocharger is investigated. Important results can be summarized as follows.

(1) In the radial turbine the centrifugal force acts against the flow direction. This causes the particles to be thrown back into the scroll. Here a physical contact with the blade seems not to be necessary. The majority of particles are thrown back under the sole effect of the centrifugal force field.

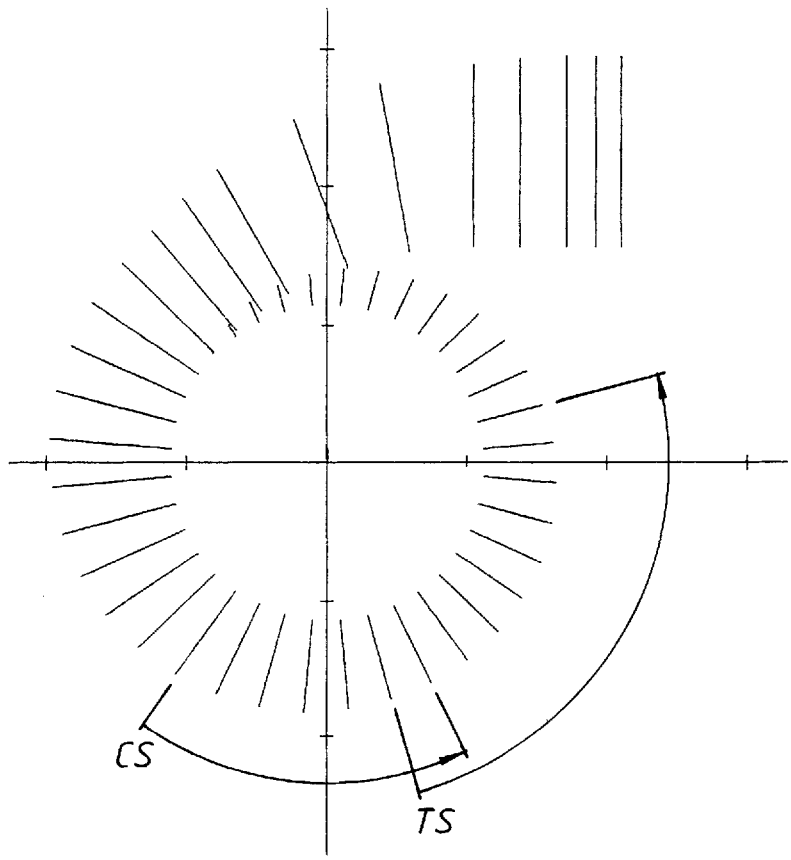

Figure 21. Regions of maximum erosion damage by re-entering particles according to case 2 results

(2) Particles are thrown back a very large number of times. The flow rate through the rotor channel seems to be extremely small (at least for initial throw-back steps) and highly sensitive to particle velocities at the rotor channel inlet. Since particles show a certain accumulation in the scroll, the neglected gas–particle and particle–particle interactions are expected to grow strongly during further throw-back steps, which may cause substantial changes in the through-flow behaviour of particles.
(3) The erosion damage in the scroll is caused not by the first-pass particles but mainly by the re-entering particles, since particles are thrown back a large number of times.
(4) Large numbers of particles move from the compressor side into the turbine side as they re-enter the scroll. This causes greater erosion damage on the turbine side of the scroll than on the compressor side.
(5) The erosion damage generally shows an increasing tendency along the scroll length, indicating maximum values near the scroll end. However, a shifting of maximum values to locations further upstream can be expected.

Several simplifying assumptions have been employed throughout the present study. However, the results indicate that some of the neglected phenomena may play important roles in reality. The neglected gas-particle and particle–particle interactions are expected to have significant

effects owing to the continuous accumulation of particles in the scroll. The turbulent dispersion of particles also seem to be important, especially for the flow behaviour of particles through the rotor channel. The neglect of the interaction of the scroll and rotor flows and the assumption of steadiness relative to the rotor in modelling the rotor channel flow do not seem to be completely justified, since the scroll outlet conditions show remarkable circumferential variations. Therefore incorporation of these phenomena in the model is expected to lead to improved predictions in future investigations.

ACKNOWLEDGEMENTS

The authors gratefully acknowledge Mr. D. Arnet, head of the department 'ZTL Technik Turbolader', for his continuous interest and support. Dr. C.-D. Schegk, the project manager, is also gratefully acknowledged for his valuable suggestions. Thanks are also due to Mr. A. Hurda, Mr. H.-P. Dickmann and Mr. P. Escher for their efforts in generating the computational grids.

APPENDIX: NOMENCLATURE

C_{REL}	relative particle speed
C_D	drag coefficient
CS	compressor side of scroll
d_P	particle diameter
r_P	radial position of particle
RC	rotor channel
Re_P	particle Reynolds number
t	time
TS	turbine side of scroll
T_{PR}	particle relaxation time
u_G, v_G, w_G	time-averaged gas velocity components in directions x_1, x_2 and x_3 respectively in stationary or rotating frame of reference
u_P, v_P, w_P	particle velocity components in directions x_1, x_2 and x_3 respectively in stationary or rotating frame of reference
U	particle speed before impact
U_N	particle velocity normal to surface relative to a stationary wall
U_T	particle velocity tangential to surface relative to a stationary wall
x_1, x_2, x_3	co-ordinates in Cartesian or cylindrical system: $x_1=x$, $x_2=y$ and $x_3=z$ for Cartesian co-ordinate system for the scroll; $x_1=x$, $x_2=r$ and $x_3=\theta$ for cylindrical co-ordinate system for the impeller

Greek letters

$\alpha_{N/T}$	restitution ratios for normal and tangential velocities
β	approach angle of particle to wall before impact
γ	equal to one for cylindrical co-ordinates; equal to zero for Cartesian co-ordinates
ε	erosion rate parameter (eroded target material per mass of impacting particles)
λ	equal to one for rotating frame of reference; equal to zero for stationary frame of reference
μ	molecular gas viscosity
ρ	density
Ω	rotational speed of rotating frame of reference

Subscripts and superscripts

G	gas
P	particle
( )′	value after impact

REFERENCES

1. J. A. C. Humphrey, 'Fundamentals of fluid motion in erosion by solid particle impacts', *Int. J. Heat Fluid Flow*, **11**, 170–195 (1990).
2. M. F. Hussain and W. Tabakoff, 'Dynamic behaviour of solid particles suspended by polluted flow in a turbine stage', *J. Aircraft*, **10**, 434–440 (1973).
3. M. F. Hussain and W. Tabakoff, 'Computation and plotting of solid particle flow in rotating cascades', *J. Comput. Fluids*, **2**, 1–15 (1974).
4. A. Hamed, 'Particle dynamics of inlet flow fields with swirling vanes', *AIAA 19th Aerospace Sciences Meeting*, St. Louis, MO, January, 1981, *Paper AIAA-81-0001*.
5. M. Mengütürk and E. F. Sverdrup, 'Calculated tolerance of a large electric utility gas turbine to erosion damage by coal ash particles', in W. F. Adler (ed.), *Erosion—Prevention and Useful Applications, ASTM Spec. Tech. Publ. 664*, 1979, pp. 193–224.
6. D. Günes and M. Mengütürk, 'Finite element computer code to calculate full 3-D compressible potential flow in turbomachinery', *International Journal of Turbo & Jet Engines*, **2**, 307–314 (1985).
7. W. Tabakoff and A. Hamed, 'Effect of environmental particles on a radial compressor', *AIAA 26th Aerospace Sciences Meeting*, Reno, NV, January 1988, *Paper AIAA-88-0366*.
8. W. Tabakoff and A. Hamed, 'Erosion problems in supercharger turbines', *Proc. 15th International Congress on Combustion Engines (CIMAC 1983)*, Paris, France, June 1983, pp. 597–611.
9. F. Boysan, W. H. Ayers and J. Swithenbank, 'A fundamental mathematical modelling approach to cyclone design', *Trans. IChemE*, **60**, 222–230 (1982).
10. A. C. Benim, 'Finite element analysis of confined turbulent swirling flows', *Int. j. numer. methods fluids*, **11**, 697–717 (1990).
11. P. J. Stopford, 'A numerical model of pulverized coal furnaces', *HFTS Rep. AERE-R 12252*, 1986.
12. C. T. Crowe, 'Review—Numerical models for dilute gas–particle flows', *J. Fluids Eng.*, **104**, 297–303 (1982).
13. A. D. Burns, I. P. Jones, J. R. Kightley and N. S. Wilkes, *Harwell-FLOW3D Release 2.1 User Manual*, CFDS, Harwell Laboratory, Abingdon, 1988.
14. R. Gebart, *Derivation of an Algorithm for Gas–Particle Flows*, RES/KBH, ABB Corporate Research Västeras, 1989.
15. B. Samuelsson, *PTRACK User Manual*, RES/KBH, ABB Corporate Research Västeras, 1989.
16. G. B. Wallis, *One-dimensional and Two-phase Flow*, McGraw-Hill, New York, 1969.
17. W. N. Dawes, 'Development of a 3-D Navier–Stokes solver for application to all types of turbomachinery', *ASME Paper 88-GT-70*, 1988.